

# Vortex pairing in the wake of a bio-inspired vehicle

Mrudhula Baskaran, Karen Mulleners\*

Institute of Mechanical Engineering, École polytechnique fédérale de Lausanne (EPFL), Lausanne, Switzerland

\*Corresponding author. E-mail:karen.mulleners@epfl.ch

## Abstract

Pulsatile jet propulsion is a highly energy-efficient swimming mode used by various species of aquatic animals that continues to inspire engineers of underwater vehicles. Here, we present a bio-inspired jet propulsor that combines the flexible hull of a jellyfish with the compression motion of a scallop to create individual vortex rings for thrust generation. Similar to the biological jetters, our propulsor generates a non-linear time-varying exit velocity profile and has a finite volume capacity. The formation process of the vortices generated by this jet profile is analysed using time-resolved velocity field measurements. The transient development of the vortex properties is characterised based on the evolution of ridges in the finite-time Lyapunov exponent field and on local extrema in the pressure field derived from the velocity data. Special attention is directed toward the vortex pairing observed in the trailing shear layer. During vortex pairing, the Lagrangian vortex boundaries first contract in the stream-wise direction before expanding in the normal direction to keep the non-dimensional energy at its minimum value in agreement with the Kelvin-Benjamin variational principle. The circulation, diameter, and translation velocity of the vortex increase due to pairing. The vortex pairing takes place because the velocity of the trailing vortex is higher than the velocity of the main vortex ring prior to merging. The comparison of the temporal evolution of the Lagrangian vortex boundaries and the pressure based vortex delimiters confirms that features in the pressure field serve as accurate and robust observables for the vortex formation process.

**Impact Statement** Aquatic animals that utilise jet propulsion intuitively manipulate the exit velocity profile and nozzle diameter in time to adapt their swimming performance. To integrate this capability in human-engineered underwater vehicles, detailed knowledge about the influence of non-linear time-varying velocity profiles on the development and formation time of vortex rings is required. We have designed a bio-inspired device that ejects propulsive vortex rings by compressing a polymer bulb to experimentally study the formation process of a vortex ring with a time-varying jet profile. Our findings reveal insight into the evolution of the integral vortex quantities for these generalised conditions and contribute to the fundamental understanding of vortex pairing in the wake of a vortex ring. The comparison of the temporal evolution of the Lagrangian vortex boundaries and the pressure based vortex delimiters confirms that features in the pressure field serve as accurate and robust observables for the vortex formation process. These results disclose new opportunities to use local pressure sensors as input for closed loop control of the temporal exit velocity profile to improve the propulsion efficiency of under water vehicles utilising pulsatile jet propulsion.

## 1. Introduction

Underwater vehicles are used for a wide range of applications, such as marine exploration (Bayat et al., 2017), ecosystem monitoring (Whitcomb et al., 2000), and ocean cleaning (Zahugi et al., 2013). One class of underwater vehicles relies on propeller-based technology and turbomachinery for long-range propulsion. These vehicles are not suitable for application in sensitive or fragile environments like coral reefs, or in constrained environments with limited space for manoeuvring (Mohseni, 2006). Another class of underwater vehicles consists of bio-inspired swimmers, which mimic the kinematics of biological organisms like fish, jellyfish, and cephalopods for locomotion (Zhu et al., 2019; Weymouth et al., 2015; Robertson et al., 2019). Bio-inspired vehicles are highly controllable and can explore a wide range of environments.

One of the mechanisms commonly exploited by bio-inspired vehicles for transport is pulsatile jet propulsion, which relies on the periodic ejection of vortex rings to create thrust (Krueger & Gharib, 2003). The canonical device used to generate and study vortex rings is the piston cylinder apparatus. A translating piston pushes fluid from within a cylinder through an opening or nozzle at the end of the cylinder where a shear layer forms and rolls-up into a coherent ring vortex (Dabiri, 2009). The vortex ring grows larger as more fluid is ejected by the piston. However, the growth of the vortex does not continue indefinitely. Beyond a limiting non-dimensional vortex formation time, additional fluid supplied by the vortex generator is no longer entrained by the vortex ring and instead forms a trailing shear layer (Gharib et al., 1998).

A vortex ring produced by a classical piston cylinder apparatus with a constant piston velocity simultaneously attains its maximum circulation, reaches its minimum non-dimensional energy, and outpaces its feeding shear layer after approximately four convective time-scales or stroke ratios (Mohseni & Gharib, 1998). This limiting value of the vortex formation time is not universal and depends on the geometry of the outlet nozzle or orifice (Limbourg & Nedić, 2021; Dabiri & Gharib, 2005), the presence of a uniform background co- or counterflow (Dabiri & Gharib, 2004; Krueger et al., 2006), and the temporal evolution of the piston velocity (Rosenfeld et al., 1998; Zhao et al., 2000; Shusser et al., 2006; Olcay & Krueger, 2010). Different time-dependent profiles of the exit velocity can noticeably alter the formation time of the ring vortex, without significantly affecting its circulation. Aquatic animals that utilise jet propulsion intuitively manipulate the exit velocity profile and nozzle diameter to adapt their swimming performance (Dabiri, 2006; Gemmell et al., 2021). The practical desire to integrate this capability in human-engineered underwater vehicles reopens fundamental questions on vortex ring formation. Detailed knowledge of the influence of arbitrary time-varying velocity profiles on the formation time and the pinch-off of vortex rings are crucial to improve the controllability and energy-efficiency of underwater vehicles that operate using jet propulsion.

An objective and frame-independent method to identify vortex pinch-off and characterise the formation process is based on Lagrangian coherent structures (Haller, 2001). Lagrangian coherent structures are maxima, or ridges, in the positive and negative finite-time Lyapunov exponent (FTLE) fields. They demarcate the vortex ring and separate regions in the flow that are dynamically different (O'Farrell & Dabiri, 2010; Shadden et al., 2006). The FTLE ridges emerge between the vortex ring and the trailing shear layer when the vortex no longer accepts additional vorticity and pinches off (Shadden et al., 2006). Alternatively, prominent features such as local extrema in the pressure field can serve as instantaneous indicators of vortex pinch-off. Regions of elevated pressure in front and behind the vortex ring are called leading and trailing pressure maxima. These maxima indicate regions where vorticity no longer passes into the vortex ring similar to the positive and negative FTLE ridges (Lawson & Dawson, 2013). The emergence of the trailing pressure maximum coincides with the formation time of the vortex ring and is a necessary condition for pinch-off (Schlueter-Kuck & Dabiri, 2016).

Here, we present a bio-inspired vortex generator as a potential propulsion mechanism for underwater vehicles. The generator consists of a soft elastic bulb that is compressed by two rigid arms. Similar

to biological jetters, our vortex generator produces a non-linear time-varying exit velocity profile and has a finite volume capacity which limits the maximum stroke length that the device can attain more than in classical piston cylinder arrangements. We experimentally study the vortex ring formation using time-resolved velocity field measurements. The transient development of the vortex characteristics are analysed based on the evolution of ridges in the finite-time Lyapunov exponent field and on local extrema in the pressure field derived from the velocity data. Special attention is directed toward the vortex pairing event observed in the trailing shear layer. The robustness of the emergence of pressure maxima as observables to identify the end of the vortex formation process is also evaluated. The findings will aid the further design and control of underwater vehicles that operate using pulsatile jet propulsion.

## 2. Materials and methods

### 2.1. Vortex generator

The bio-inspired vortex generator designed for this study combines the flexible bell of a jellyfish (Weymouth et al., 2015; Xu, 2021) with the bivalve compression of a scallop (Robertson et al., 2019). The generator presented in Figure 1 produces vortex rings by compressing an elastic bulb with two rigid arms and ejecting fluid through a circular nozzle with diameter  $D = 14$  mm. The silicon bulb is prepared by mixing a silicone moulding compound (Zhermack Elite Double 32 shore A base) and a catalyst in a 1:1 ratio and centrifuging the mixture. The mixture is then poured into a plastic mould prescribing the shape of the bulb and rotated slowly for 30 minutes to ensure a homogeneous thickness of 1.5 mm across the bulb. The bulb has a volume of 150 mL when uncompressed (Figure 1b). The body and arms of the vortex generator are 3D printed with standard clear resin using a stereolithographic printer (Formlabs Form 2). The motion of both arms is controlled by a brushless servo motor (Maxon EC-max) along a single motor shaft via the use of a gear box, which ensures symmetrical compression of the bulb (Figure 1a). Commands to the motor are sent via a motor controller (DMC-4040, Galil Motion Control, USA).

### 2.2. Experimental setup

The vortex generator is placed in a rectangular glass tank filled with water. Time-resolved particle image velocimetry (PIV) is used to measure the velocity field in a stream-wise symmetry plane of the vortex.

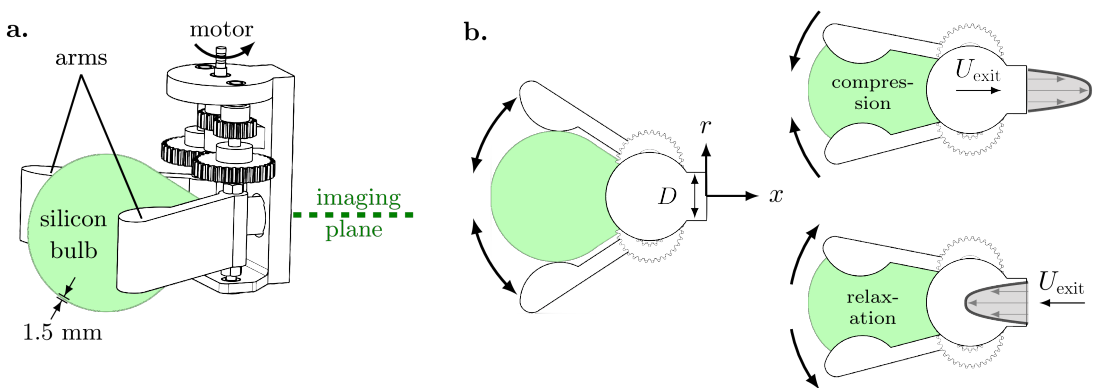


**Figure 1.** (a.) Schematic of the vortex generator including the gear system to translate the rotation on the main axis into a symmetric compression of the bulb by the two arms. (b.) Relaxed and compressed states of the bulb.

Polystyrene particles with a diameter of 56  $\mu\text{m}$  are used as seeding particles. The starting position of the arms is the angle at which they touch the bulb without compressing it (Figure 1b). The angle of the arms is varied with a sinusoidal profile, to smoothly compress and relax the bulb with a prescribed amplitude and time period. The bulb walls are thick enough such that the material does not stretch upon mechanical compression by the arms. The arms mechanically limit the volume the bulb can contain. When the arm are opened, the bulb returns to its original form. Two high-power light-emitting diodes (LED) (LED Pulsed System, ILA\_5150 GmbH, Germany) create a light sheet in the horizontal stream-wise plane cutting through the centre of the exit nozzle (Figure 1a). The applicability of these high-power LED for PIV has been demonstrated previously by Buchmann et al. (2012); Krishna et al. (2018). The LED are operated in continuous mode during image acquisition. A mirror angled at  $45^\circ$  is placed underneath the tank and a high-speed camera (Photron Fastcam SA-X2) records  $1024 \text{ px} \times 512 \text{ px}$  images with an acquisition rate of 2000 Hz. The start of the PIV image acquisition coincides with the start of the compression of the vortex generator. Consecutive particle images are correlated using a multigrid evaluation method with an initial window size of  $32 \text{ px} \times 32 \text{ px}$  and step size of 3 px, or 90 % overlap. This corresponds to a physical grid spacing of 0.21 mm or 0.015 D.

### 2.3. Finite-time Lyapunov exponent field and ridge computation

The candidate material boundaries of the generated ring vortex are identified from ridges in the finite-time Lyapunov exponent field (FTLE). The FTLE fields are calculated directly from the measured time-resolved velocity fields by artificially seeding and convecting fluid particles forward or backward in time to obtain the forward or positive pFTLE and backward or negative nFTLE fields. The initial position of the fluid particle is indicated by  $\mathbf{x}$  and their positions after a given integration time  $T_f$  are found by advecting the particles with the flow using a fourth order Adam-Bashforth-Moulton integration scheme. The flow map  $\phi_t^{t+T_f}$  describes the displacement of the particles between time  $t$  and  $t + T_f$ . The spatial gradient of the flow map gives us the Cauchy-Green strain tensor whose largest eigenvalue ( $\lambda_{\max}$ ) is referred to as the coefficient of expansion  $\sigma^{T_f}(\mathbf{x}, t)$  (Green et al., 2010). The scalar FTLE field is then defined as (Haller, 2002):

$$\text{FTLE}^{T_f}(\mathbf{x}, t) = \frac{1}{2T_f} \ln \left( \lambda_{\max} \left( \left[ \nabla \phi_t^{t+T_f} \right]^* \left[ \nabla \phi_t^{t+T_f} \right] \right) \right) = \frac{1}{2T_f} \ln \left( \sigma^{T_f}(\mathbf{x}, t) \right) \quad (1)$$

where  $*$  is the matrix transpose operator.

Candidate vortex boundaries manifest as ridges or maxima of the scalar FTLE field (Haller, 2002; Shadden et al., 2006; Green et al., 2007, 2010). Ridges in the positive FTLE field are candidate repelling material lines and correspond to regions where there is a maximum divergence of fluid particle trajectories over time. Ridges in the negative FTLE field are candidate attracting material lines and correspond to regions where there is maximum attraction of fluid particle trajectories over time. The ridges are computed here using a ridge tracking algorithm. The algorithm locates grid points with maximum intensity and performs a search within the adjacent grid points to determine the next point on the ridge. An adjacent grid point is selected as the next ridge point if it has a similar or larger magnitude of the finite-time Lyapunov exponent than the current grid point. The integration time  $T_f$  used for the data presented here is 0.4 s or 80 % of the full compression-relaxation cycle.

### 3. Results and discussion

#### 3.1. Fluid ejection and entrainment

Our vortex generator operates by compressing and relaxing its deformable bulb. Compression ejects fluid into the wake and relaxation entrains fluid by allowing the bulb to return to its original form. The temporal evolution of the average velocity of the fluid that is ejected or entrained by the propulsor is obtained by integrating the vertical velocity profile directly behind the nozzle exit of the propulsor. This average exit velocity across the nozzle diameter  $D$  is defined in cylindrical coordinates as

$$U_{\text{exit}}(t) = \frac{4}{\pi D^2} \int_0^{2\pi} \int_0^{D/2} u(r, x=0, t) r \, dr \, d\theta \quad (2)$$

where  $u(r, x=0, t)$  is the stream-wise velocity component directly behind the nozzle exit at  $x/D = 0$ . Schematic representations of the velocity profiles at the nozzle exit and the temporal evolution of the averaged exit velocity are presented in [Figure 2](#) over the duration of one compression-relaxation cycle  $T$ . Positive and negative values of the exit velocity  $U_{\text{exit}}$  correspond respectively to fluid ejection and fluid entrainment. The exit velocity  $U_{\text{exit}}$  in [Figure 2](#) is normalised by  $U_0$ , the characteristic velocity of the system, which is defined as

$$U_0 = \frac{8V_0}{\pi D^2 T} \quad (3)$$

Here,  $V_0$  is the total volume of fluid ejected from the propulsor during the duration of bulb compression,  $T/2$ . The velocity  $U_0$  is the velocity of the equivalent constant uniform flow that yields the same ejected volume of fluid over the time of bulb compression. The Reynolds number  $Re_D$  based on the nozzle exit diameter and  $U_0$  is 5820 for the data presented here.

Due to the particular design of our vortex generator, the exit velocity increases slowly when the compression starts, but rapidly catches up and reaches a maximum value of  $U_{\text{exit}}/U_0 \approx 1.9$  at  $t/T = 0.13$ . At  $t/T = 0.5$ , the kinematics of the propulsor cause a transition from bulb compression to bulb relaxation. The fluid does not respond directly to the transition of the kinematics and continues to flow out of the bulb for  $\Delta t/T \approx 0.07$  after bulb relaxation has begun. A shorter lag in the response of the flow with respect to the forcing kinematics is present at the end of cycle. The flow continues to be entrained for  $\Delta t/T \approx 0.04$  after the driving kinematics have stopped. The slight asymmetry in the fluid ejection-entrainment response to the symmetric compression-relaxation motion is characteristic of this particular driving kinematics and could be compensated for or enhanced by using more complex kinematics.

The length of an equivalent cylindrical column of fluid ejected by the vortex propulsor during compression and relaxation is called the stroke length. It is defined here as:

$$L(t) = \int_0^t U_{\text{exit}}(\tau) \, d\tau \quad (4)$$

The stroke length is analogous to the distance travelled by the piston in a piston cylinder apparatus to eject the same volume of fluid. The temporal evolution of the stroke to diameter ratio  $L/D$  is presented in [Figure 2f](#). After the initial slow response of the flow to the compression kinematic, the stroke ratio increases non-linearly during the compression phase for  $0 < t/T < 0.57$ . The stroke ratio attains a maximum value of 7 around  $t/T = 0.57$  and decreases approximately linearly with a rate  $dL/dt = -5.7D/T$  during the relaxation phase for  $0.57 < t/T < 1.04$ .

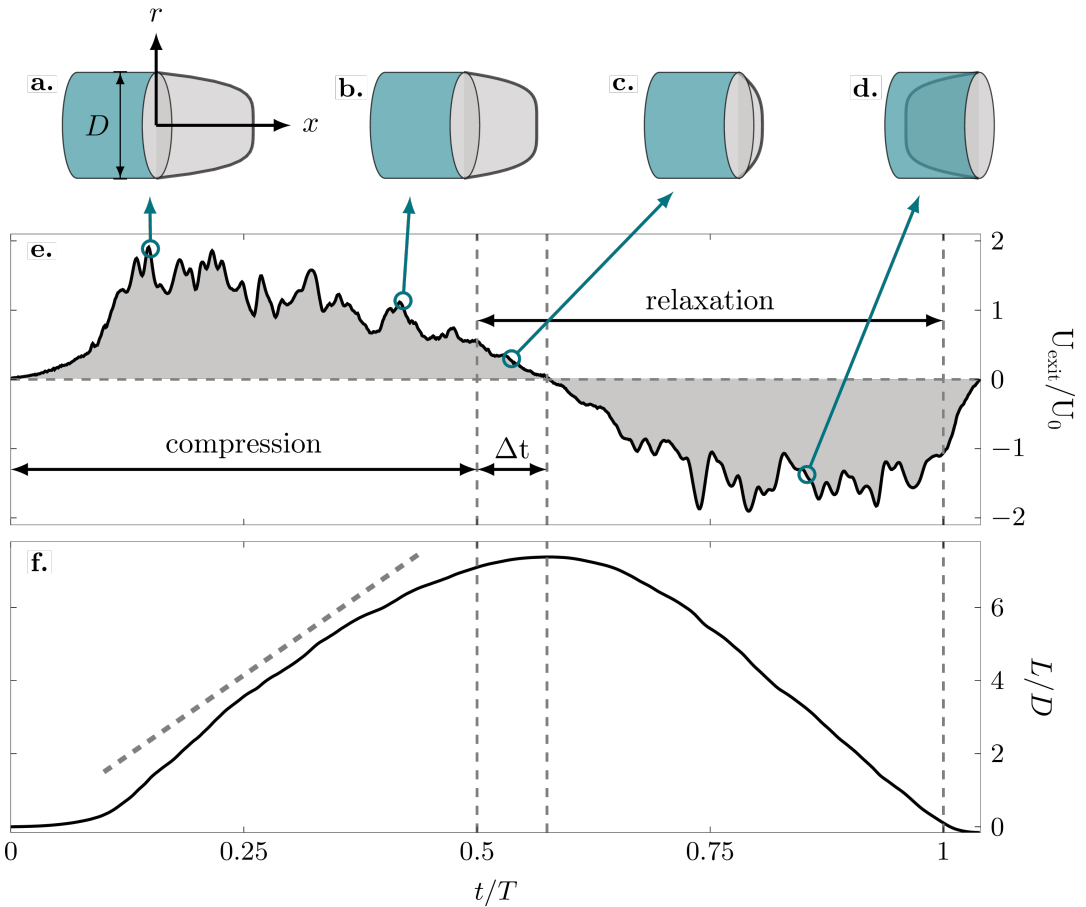


**Figure 2.** (a)-(d) Reference cylindrical coordinate system and schematics of the velocity profiles at the nozzle exit at different times during the compression-relaxation cycle. Fluid leaving the nozzle moves in the positive  $x$ -direction which is referred to as the stream-wise direction. (e) Temporal evolution of the measured diameter averaged exit velocity  $U_{\text{exit}}$  normalised by the characteristic velocity  $U_0$  over the duration of one compression-relaxation cycle  $T$ . (f) Non-dimensional stroke ratio obtained from integrating  $U_{\text{exit}}$  in time.

The temporal velocity profile of the fluid ejected by the vortex generator is not constant and leads to a non-linear variation of the stroke ratio. This allows us to characterise the formation process of a vortex ring generated by a non-linear evolution of the stroke ratio, which has not yet received much attention. In addition to the nonlinear fluid ejection profile, the fluid entrainment process is unique to the design of our propulsor, and enables the periodic ejection of multiple vortex rings. The effect of the time-varying exit velocity profile and the fluid entrainment process on the temporal evolution of the propulsion force will be the subject of future investigations. Here, we focus solely on the flow field created by our propulsor. Our goal is to characterise the formation process of a vortex ring generated by the arbitrary fluid ejection profile and identify observable quantities that can aid a future optimisation of similar robotic devices that utilises pulsatile jet propulsion.

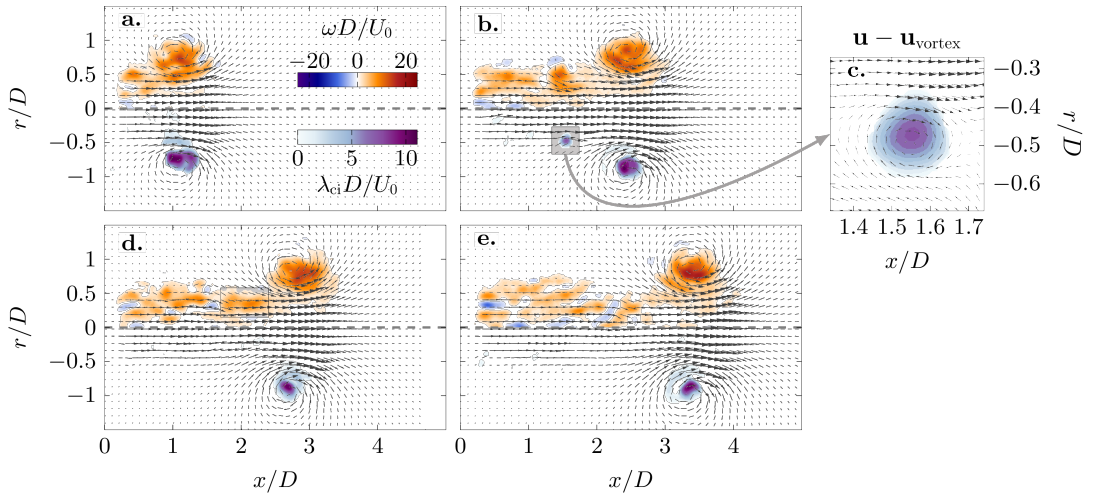


**Figure 3.** Snapshots of experimentally observed vortex ring development during the compression phase of the vortex generator at (a)  $L/D = 3.4$ , (b,c)  $L/D = 5.0$ , (d)  $L/D = 5.5$ , and (e)  $L/D = 5.9$ . The colours in the top half of the snapshots indicate values of the experimentally measured out-of-plane vorticity component  $\omega$ . The colours in the bottom half of the snapshots indicate the experimentally obtained swirling strength  $\lambda_{ci}$ . (c) Zoomed-in view on a secondary vortex in the trailing shear layer with velocity vectors indicating the relative velocity with respect to the centre of the secondary vortex. The vorticity associated with the secondary vortex in (d) is indicated by the small box.

### 3.2. Vortex formation process

When fluid is ejected by our vortex propulsor a coherent vortex ring is formed. The growth of the vortex ring is presented by instantaneous snapshots of the flow field in Figure 3. The arrows represent the two dimensional velocity field  $(u, v)$  in the measurement plane. The out-of-plane vorticity component,  $\omega$ , is computed from the in-plane velocity field and is show in the top half of the snapshots in Figure 3. The colours in the bottom half of the snapshots indicate the swirling strength,  $\lambda_{ci}$ , which is the imaginary part of the complex eigenvalues of the velocity gradient tensor (Zhou et al., 1999). The swirling strength is a robust indicator of vortices in shear layers where high concentrations of vorticity exist and obfuscate the presence or absence of vortices.

The shear layer that emerges at the boundary between the ejected fluid and the surrounding quiescent flow immediately rolls-up into a vortex ring. The coherent core is indicated by localised region of non-zero values of the swirling strength (Figure 3a). The vortex ring rapidly convects away from the nozzle exit while flow is still being ejected and a trailing shear layer appears between the vortex ring and the nozzle exit (Figure 3b). At  $L/D = 5$ , a secondary or trailing vortex is present in the trailing shear layer. Based on the vorticity concentration alone, it is difficult to distinguish between a strong shear flow and rotation, but the swirling strength distribution is conclusive (Figure 3b,c). This secondary vortex core is not persistent and is no longer visible in the swirling strength field for  $L/D > 5.5$  when the primary vortex travels further downstream and moves away from the trailing shear layer (Figure 3d-e). The vorticity associated with the secondary vortex is still present and has moved closer to the primary vortex (indicated by the box in Figure 3d) suggesting that the primary and secondary vortices are merging.

To confirm the pairing of the primary and secondary vortices, we analyse the temporal evolution of the Lagrangian coherent structures in the positive and negative finite-time Lyapunov exponent (FTLE) fields, which mark the boundaries of the vortex. Figure 4 shows the positive and negative FTLE ridges and fields atop the vorticity and swirling strength fields. The positive ridge is the upstream boundary

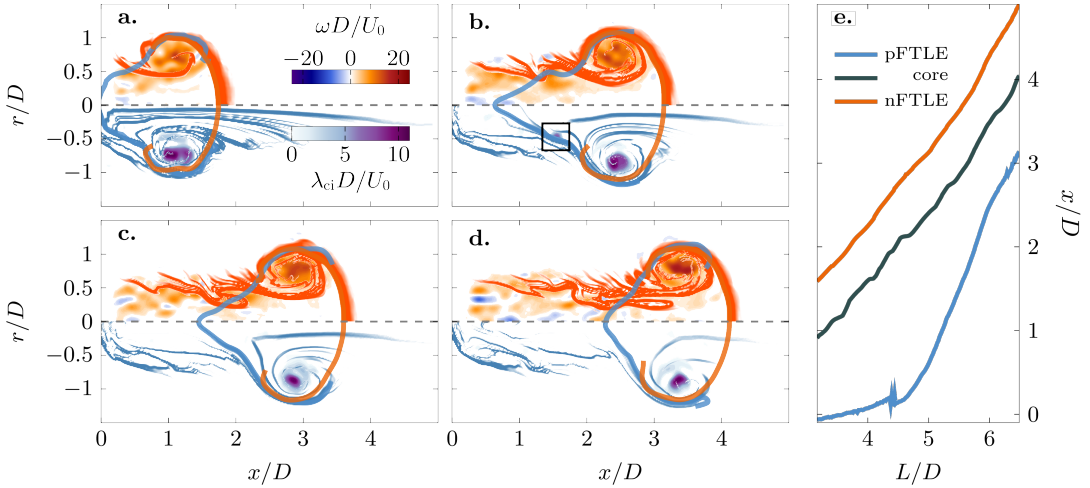


**Figure 4.** Positive and negative finite-time Lyapunov exponent (FTLE) ridges, computed from experimental data, indicating the boundaries of the vortex ring presented atop the vorticity and  $\lambda_{ci}$  fields for (a)  $L/D = 3.4$ , (b)  $L/D = 5.0$ , (c)  $L/D = 5.5$ , and (d)  $L/D = 5.9$ . (e) Evolution of the stream-wise location of the vortex core and of the crossing of the positive and negative FTLE ridges with the centreline as a function of the stroke ratio.

of the vortex ring along which particle trajectories are attracted. The negative ridge is the downstream boundary of the vortex ring from which particle trajectories are repelled. The two ridges can be identified once the core of the primary vortex ring has moved one nozzle diameter away from the exit. The evolution of the stream-wise location of the vortex core and of the intersections of the positive and negative FTLE ridges with the centreline are presented as a function of the stroke ratio  $L/D$  in Figure 4e. As the vortex convects away from the nozzle exit, the positive FTLE ridge lags behind the vortex core (Figure 4b,e). The positive FTLE ridge encloses the secondary vortex core indicated by the box in Figure 4b. For  $L/D > 5$  the positive FTLE ridge accelerates and catches up with the vortex core, pushing the vorticity associated with the secondary vortex core to merge with the vorticity of the primary core. The distance between the positive FTLE ridge and the core reaches a steady state at  $L/D \approx 6$  such that the Lagrangian boundaries symmetrically enclose the vortex core (Figure 4d).

The evolution of the positive ridge during vortex pairing enables the mixing of two dynamically different regions of fluid: fluid inside the primary vortex ring and fluid that is in the trailing shear layer including the secondary vortex ring (O’Farrell & Dabiri, 2010). At the end of pairing, the positive and negative FTLE ridges are symmetric with respect to the vortex core and the vortex ring has separated from the trailing shear layer. A symmetric definition of the vortex ring by the FTLE ridges matches the intuitive idea of a pinched-off vortex ring, with the ridges acting as physical barriers that prevent the entrance of additional vorticity into the ring.

### 3.3. Evolution of vortex topology during vortex pairing

The distance between the intersections of the positive and negative FTLE ridges with the centreline is used to define the stream-wise length,  $L_o$ , of the vortex. The largest distance in the radial direction between the topmost and bottommost points on the positive FTLE ridge is used here to define the outer diameter,  $D_o$ , or height of the vortex. The definition of these vortex shape characteristics are indicated in Figure 5a and their temporal evolution for  $L/D > 3$  is presented in Figure 5b. For lower stroke ratios, we can not yet identify the downstream FTLE ridge to determine the vortex length.

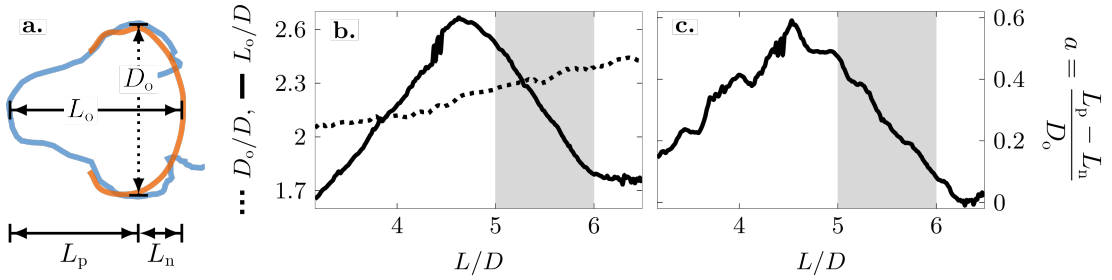


**Figure 5.** Evolution of the shape and asymmetry of the experimentally observed vortex ring. (a) Vortex boundaries indicated by the FTLE ridges including the definition for the vortex stream-wise length and outer diameter. Temporal evolution of the (b) vortex length and outer-diameter and (c) the asymmetry parameter  $a$  as defined by Equation (5) as a measure for the degree of asymmetry of the FTLE boundaries with respect to the vortex core. The shaded area indicates when vortex pairing occurs.

Around  $L/D = 3$ , the vortex outer diameter is about twice the nozzle diameter and larger than the stream-wise length. The outer diameter increases approximately linearly during the rest of the compression phase of the bulb to  $D_o = 2.4 D$  at  $L/D = 6.5$ . The stream-wise length increases faster than the outer diameter as the positive FTLE ridge lags behind and reaches a maximum value of  $L_o = 2.65 D$  at  $L/D \approx 4.6$ , yielding a minimum aspect ratio of  $L_o/D_o = 0.8$ . For  $L/D > 4.6$ , the positive FTLE ridge starts catching up with the vortex core and negative ridge (Figure 4c) and the stream-wise length rapidly decreases and converges to a value of  $L_o = 1.76 D$  for  $L/D > 6$ . This corresponds to an aspect ratio of  $L_o/D_o = 1.4$ . Based on the velocity field (Figure 3) and FTLE snapshots (Figure 4), the pairing of the secondary vortex with the primary vortex ring occurs for  $5 < L/D < 6$ . During this time interval, indicated by the shaded region in Figure 5b, the FTLE boundaries contract and push vorticity from the tail of the FTLE bound region towards the primary core line to merge.

To quantify the asymmetry of the FTLE bound area with respect to the vortex core location, we introduce the following asymmetry parameter:

$$a = \frac{L_p - L_n}{D_o} \quad , \quad (5)$$

with  $L_n$  the distance from the stream-wise location of the vortex core to the leading nFTLE intersection, and  $L_p$  the distance from the stream-wise location of the vortex core to the lagging pFTLE intersection with the centreline (Figure 5a). Values of  $a$  close to zero indicate symmetric FTLE boundaries with respect to the vortex core, higher positive values indicate an asymmetric tail heavy FTLE enclosed area. For  $3 < L/D < 4.5$ , the asymmetry increases similarly to the vortex length due to the lagging of the positive FTLE ridge. For  $L/D > 4.5$ , the positive FTLE ridge catches up with the core line and the asymmetry parameter decreases and reaches zero at  $L/D = 6.2$ . The FTLE boundaries become fully symmetric with respect to the vortex core after vortex pairing.

### 3.4. Evolution of integral quantities during vortex pairing

The variation in the vortex ring topology during pairing affects the amount of vorticity and its distribution inside the vortex core, which influences the vortex circulation, hydrodynamic impulse, and energy (Gharib et al., 1998; de Guyon & Mulleners, 2021b). The circulation of the vortex ring is computed as

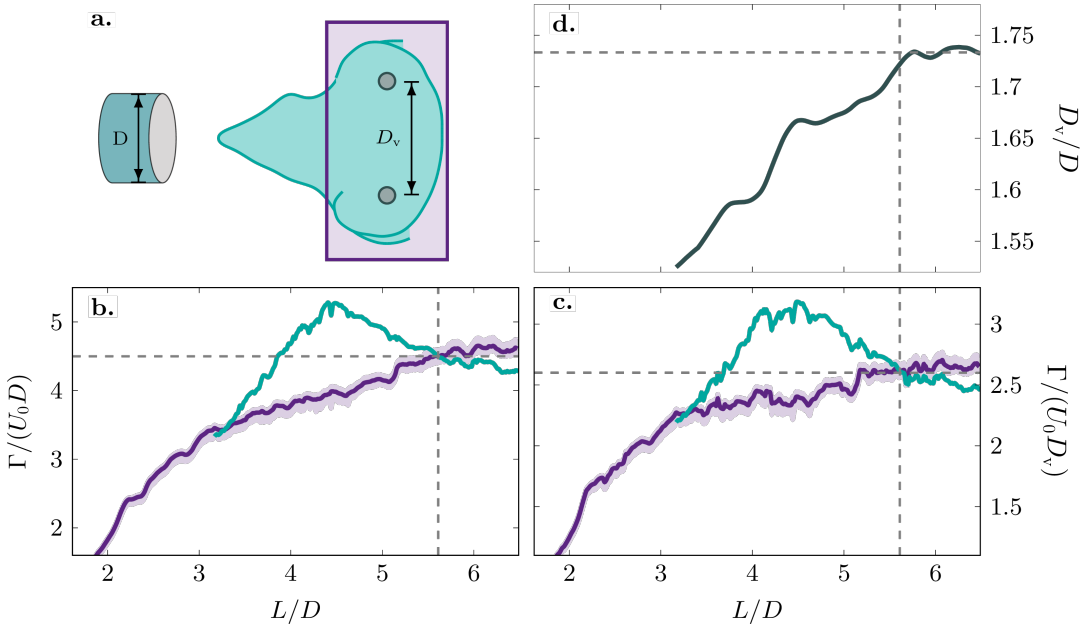


**Figure 6.** Temporal evolution of the vortex circulation and vortex diameter. Circulation values obtained by integration of the experimentally obtained out-of-plane vorticity within the area bound by the positive and negative FTLE ridges are presented in violet, values obtained by integration within a rectangular box centred around the primary vortex centres are presented in turquoise. The light blue shaded region represents the uncertainty based on variations in the box height. (a) Sketch of the two integration areas. (b) Circulation normalised by  $U_0$  and the nozzle diameter  $D$ . (c) Circulation normalised by  $U_0$  and the vortex diameter  $D_v$ . (d) Evolution of the vortex diameter normalised by the nozzle diameter.

the surface integral of the average between the positive and negative out-of-plane vorticity:

$$\Gamma = \iint_A \frac{|\omega|}{2} dA \quad . \quad (6)$$

We have calculated the circulation within the area bound by the FTLE ridges and within a rectangular area centred around the vortex centre such that it only contains the primary vortex ring (Figure 6a). The temporal evolution of the non-dimensional circulation in both integration areas is presented in Figure 6b,c. The circulation is non-dimensionalised by the characteristic velocity  $U_0$  and the nozzle outlet diameter  $D$  in Figure 6b and by  $U_0$  and the vortex diameter  $D_v$  in Figure 6c. The vortex diameter normalised by the nozzle diameter is presented in Figure 6d.

Due to the initial tail-heavy asymmetry of the FTLE boundaries with respect to the vortex core, the circulation inside the FTLE contour is higher than the circulation in the box until  $L/D \approx 5.5$ . The width of the FTLE boundary converges to the width of the rectangular contour post vortex pairing and the two circulation curves in Figure 6b,c converge to  $\Gamma/(U_0 D) \approx 4.3$  and  $\Gamma/(U_0 D_v) \approx 2.5$ . The final value of the vortex circulation when normalised by the vortex diameter instead of the nozzle diameter is close to the non-dimensional values reported for propulsive vortex rings generated with a piston cylinder (Gharib et al., 1998) and drag vortices behind a translating cone (de Geyon & Mulleners, 2021b).

The difference between the circulation in the FTLE contour and in the rectangular contour for  $L/D > 5.5$  is attributed to vorticity outside the FTLE contour in radial direction. For  $L/D < 5.5$ , the difference is attributed to circulation in the trailing shear layer that will eventually be fed into the primary vortex ring

through pairing. The maximum circulation in the FTLE boundary is measured when the stream-wise length of the vortex is also maximal (Figure 5b). The circulation in the rectangular contour gradually increases during the entire compression phase and does not attain a local maximum prior to converging at  $L/D > 5.5$ . When the circulation inside the vortex ring is normalised by the vortex diameter instead of the nozzle diameter, the non-dimensional circulation already reaches 90 % of its final value after  $L/D = 3.6$ , which is well before vortex pairing takes place. The additional volume and associated vorticity that is added to the main vortex ring due to merging does not significantly alter the non-dimensional circulation based on the vortex size, but primarily leads to an increase in the vortex core diameter (Figure 6d). The vortex core diameter converges to  $D_v/D = 1.73$  at the same time as the non-dimensional circulation.

The non-dimensional energy of the vortex ring serves as a measure for the distribution of the vorticity inside the vortex ring (de Guyon & Mulleners, 2021b). According to Gharib et al. (1998), the non-dimensional energy  $E^*$  is defined as:

$$E^* = \frac{E}{\sqrt{\rho} \Gamma^3} \quad . \quad (7)$$

with  $E$  the kinetic energy,  $\rho$  the fluid density,  $I$  the impulse, and  $\Gamma$  the circulation of the vortex ring. The kinetic energy is computed as:

$$E = \pi \rho \iint_A \omega \psi dA \quad , \quad (8)$$

where  $\psi$  is the stream function, obtained from integrating the Cauchy Riemann equations for the axis-symmetric vortex ring, and  $A$  the integration area. We have computed the integral again in the area bound by the FTLE ridges and within a rectangular area centred around the vortex centres, similar to the procedure applied to compute the circulation (Figure 6a). The impulse of the vortex ring is computed as:

$$I = \pi \rho \iint_A \omega |r|^2 dA \quad , \quad (9)$$

where  $|r|$  is the distance away from the vortex centreline.

The non-dimensional energy for the two integration areas is presented in Figure 7a. The evolution of  $E^*$  within the FTLE boundary is only shown as a reference. Due to the asymmetric shape of the FTLE boundaries for  $L/D < 6$ , we can not interpret the value of non-dimensional energy as a measure of the vorticity distribution within this contour. The non-dimensional energy inside the rectangular contour that contains only the primary vortex ring drops to a steady state value of 0.26 after only three stroke ratios. The initial decrease in  $E^*$  indicates the evolution towards a uniform vorticity distribution (de Guyon & Mulleners, 2021b). The limit value falls within the range of typical limit values observed for vortex rings generated under various conditions (Gharib et al., 1998; Nitsche, 2001; Limbourg & Nedić, 2021). The additional volume and circulation that will merge with the primary vortex ring at later times does not alter its non-dimensional energy. This is a great example of the Kelvin-Benjamin variational principle which states that a vortex will only accept additional vorticity if this maximises the impulse-normalised energy of the new configuration (Benjamin, 1976). The primary vortex is able to accept the additional vorticity from the secondary vortex by increasing its radius and redistributing the vorticity such that its non-dimensional energy remains constant.

The reason the secondary vortex can pair with the primary vortex in the first place is due to their relative translation velocity. The vortex translation velocity is calculated from the non-dimensional energy,

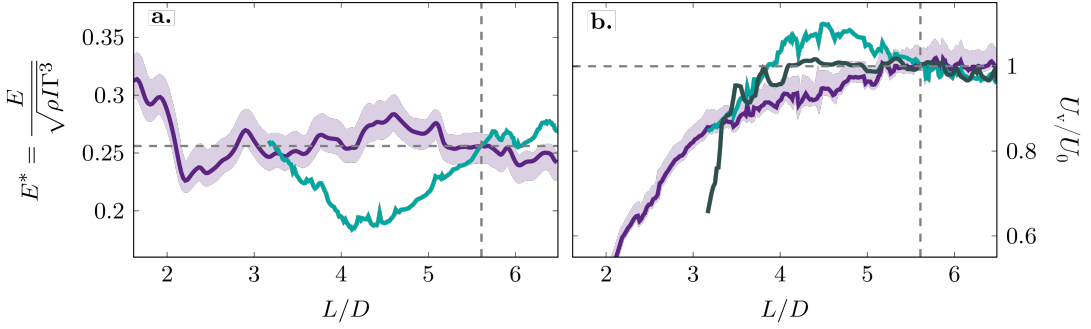


**Figure 7.** Temporal evolution of (a) the non-dimensional energy of the vortex and (b) the translational velocity of the experimentally observed vortex according to Equation (10) and based on the tracking of the vortex centre locations. Values obtained by integration in the area bound by the FTLE ridges are presented in violet, values obtained by integration within a rectangular box centred around the vortex centres are presented in turquoise.

circulation, and diameter of the vortex ring (Akhmetov, 2009; de Guyon & Mulleners, 2021b):

$$U_v = \frac{\Gamma}{\pi D_v} \left( E^* \sqrt{\pi} + \frac{3}{4} \right) . \quad (10)$$

The temporal evolution of the translational velocity based on the integral values computed for the FTLE boundary and the rectangular contour enclosing solely the primary vortex is presented in Figure 7b. The translational velocity based on the tracking of the vortex centres is included in Figure 7b for comparison. The translational velocity of just the primary vortex ring based on the integral quantities rapidly increases during the first three stroke ratios to a value of  $U_v/U_0 = 0.8$ . The velocity based on the tracking the core converges to  $U_v/U_0 = 1$  after four stroke ratios. This rapid increase in the translational velocity causes the core to move away from the nozzle exit. At  $L/D = 3$ , the core has already move one diameter away from the outlet (Figure 4a,e) which makes it harder to directly feed additional vorticity into the primary vortex, but it does not mean that the vortex is not able to accept additional vorticity at a later stage. The early physical distancing of the primary vortex ring is a direct consequence of the specific time-varying outlet velocity profile of our vortex generator.

The translational velocity based on the integral values computed for the FTLE boundary increases beyond the velocity of the primary vortex for  $4 < L/D < 5.5$ . This difference is attributed to the higher translational velocity of the secondary vortex in the tale of the FTLE bounded area. The secondary vortex catches up with the primary vortex and they pair. The vortex diameter, circulation, and translational velocity all converge to new post-pairing values for  $L/D > 5.5$  while the non-dimensional energy remains at its limiting pre-pairing value in agreement with the Kelvin-Benjamin variational principle.

### 3.5. Fluid entrainment and detrainment during vortex pairing

The entrainment and detrainment of fluid into the pairing of the primary and secondary vortex is visualised using a Lagrangian approach. Artificial seed particles are placed inside and outside the vortex boundaries marked by the FTLE ridges  $L/D = 3.7$  and are convected with the flow. The initial time of particle seeding is selected such that the FTLE ridges demarcating the vortex have fully formed and form a closed contour. The locations of the seed particles at different time instants during the compression stage of the bulb are presented in Figure 8. The top half of the snapshots in Figure 8 present the results for particles that were initially inside the FTLE boundaries and show fluid detrainment. The bottom

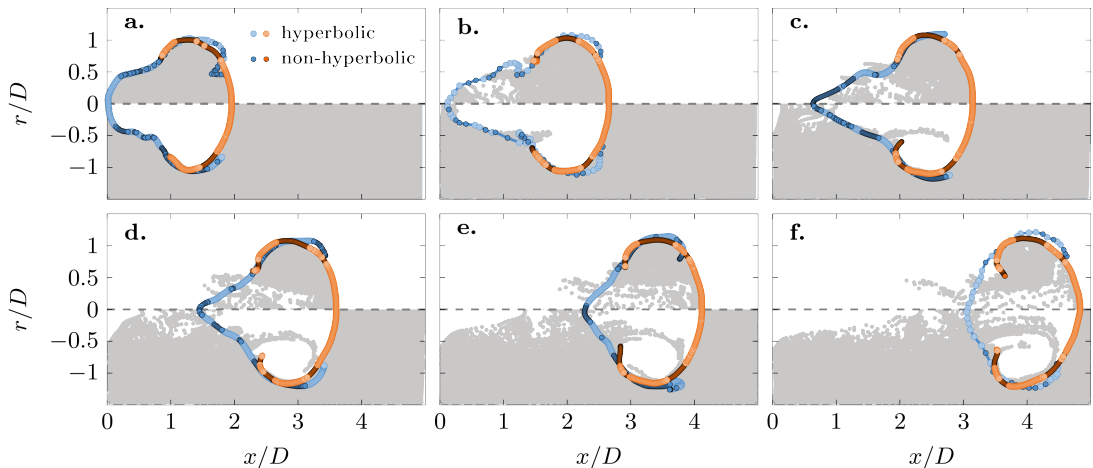


**Figure 8.** Snapshots of artificial seed particles convected by the experimentally measured flow. Top half show particles initially inside the FTLE boundaries, bottom half show particles initially outside the FTLE boundaries. White symbols correspond to points along the FTLE ridges that are non-hyperbolic, filled coloured symbols correspond to points along the FTLE ridges that are hyperbolic. Initial position of the particles at (a)  $L/D = 3.7$ , and their location after convection by the flow at (b)  $L/D = 4.4$ , (c)  $L/D = 5.0$ , (d)  $L/D = 5.5$ , (e)  $L/D = 5.9$ , and (f)  $L/D = 6.4$ .

half of the snapshots in Figure 8 present the results for particles that were initially outside the FTLE boundaries and show fluid entrainment.

By definition, fluid particles move around the negative ridge and are attracted by the positive FTLE ridge (Haller, 2002; Shadden et al., 2007). Occasionally, particles surpass the positive FTLE ridge to enter the vortex boundary (Figure 8d-f). The particles leave through the formation of lobes in the negative FTLE ridge, in the process known as tail shedding (Shadden et al., 2006; de Guyon & Mulleners, 2021a).

To understand how particles can cross FTLE ridges we compute the strain rates normal to the ridges. The strain rates allow us to verify whether the ridges are indeed hyperbolic Lagrangian coherent structures (Haller, 2002; Green et al., 2010). The positive FTLE ridge, which repels particles, is a hyperbolic repelling material line if the strain rate normal to the ridge is positive. A negative FTLE ridge is an attracting material line if the strain rate normal to the ridge is negative (Haller, 2001). The sign of the strain rates on the positive and negative FTLE ridges are indicated by the markers in Figure 8. The negative FTLE ridge continuously maintains negative strain rates on the ridge throughout the process, confirming that it is a hyperbolic attracting material line (Green et al., 2007). The entrainment of fluid particles into the vortex ring across the positive FTLE ridges occurs where the ridges are locally non-hyperbolic (Figure 8b-e). The positive FTLE ridge evolves into an entirely hyperbolic repelling ridge post vortex pairing when the ridges symmetrically enclose the primary vortex core (Figure 8f).

### 3.6. Evolution of pressure field during vortex pairing

The Lagrangian analysis provides detailed and accurate insight into the formation and development of the vortex ring generated by our propulsor. But, the Lagrangian analysis is computationally expensive, requires time resolved flow field data, and is not suitable for in-situ optimisation and control of the time-dependent exit velocity profile. Local instantaneous pressure measurements would be preferential for this purpose. To evaluate the potential of pressure-based indicators of vortex formation we need to explore how pressure features in the flow field related to the previously extracted Lagrangian boundaries.

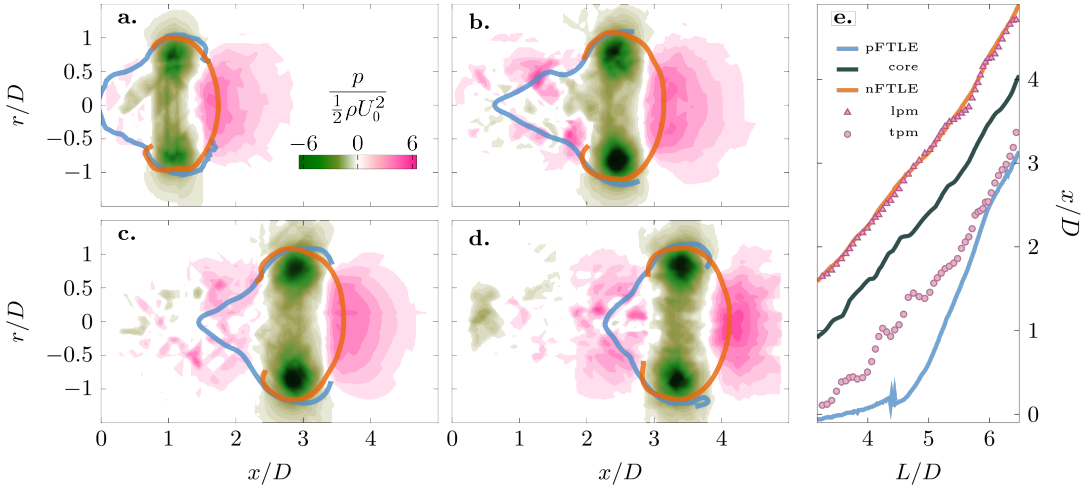


**Figure 9.** Snapshots of the pressure field derived from the experimentally measured velocity field at (a)  $L/D = 3.4$ , (b)  $L/D = 5.0$ , (c)  $L/D = 5.5$ , and (d)  $L/D = 5.9$ . (e) Evolution of the stream-wise location of the vortex core, of the crossing of the positive and negative FTLE ridges with the centreline, and of location of the leading and trailing pressure maxima (lpm, tpm) along the centreline as a function of the stroke ratio.

The pressure field is computed from a direct integration of the velocity field (Dabiri et al., 2014) and presented in Figure 9 for selected snapshots. The FTLE ridges are added atop the pressure fields for comparison. The pressure minima reliably indicate the location of the vortex core in all the snapshots. The pressure minimum becomes stronger with increasing stroke ratio. A high pressure region called the leading pressure maximum forms ahead of the vortex core and has a local maximum where the negative FTLE ridge intersects with the centreline (Figure 9a). Local high pressure regions or trailing pressure maxima, emerge aft of the primary vortex core for  $L/D > 3.5$ . These regions are scattered pre vortex pairing (Figure 9b,c) and combine to a single more coherent region centred around the intersection of the positive FTLE ridge with the centreline post pairing (Figure 9d).

The evolution of the stream-wise locations of the vortex core, of the intersection of the positive and negative FTLE ridges with the centreline, and of the location of the leading and trailing pressure maxima along the centreline are summarised in Figure 9e. The trajectory of the leading pressure maximum and the negative FTLE ridge coincide perfectly. The trailing pressure maximum is initially ahead of the positive FTLE ridge which lags behind the primary vortex core. For  $4.4 < L/D < 6$ , the trailing pressure maximum cannot be reliably identified in all snapshots. We use a linear interpolation to fill the gaps. The locations of the trailing pressure maximum and the positive FTLE ridge match closely post-pairing.

The leading and trailing pressure maxima, like the positive and negative FTLE ridges, reliably indicate the upstream and downstream bounds of the vortex ring (Lawson & Dawson, 2013). The ridges and the pressure maxima symmetrically enclose the primary vortex core and act as physical barriers that prevent additional fluid from entering the vortex ring. The pressure maxima can serve as reliable observables for vortex ring formation and shedding that can be used for future optimisation and control of the driving jet profile of bio-inspired vehicles and other vortex generating systems. A pressure-based methodology does not require time-resolved data and is computationally less expensive than calculating the FTLE field. Our results disclose new possibilities to incorporating pressure sensors and probes in the flow to measure vortex ring properties in-situ.

## 4. Conclusion

We have presented here a bio-inspired jet propulsor that combines the body morphologies of two marine organisms, the bell muscle of the jellyfish and the compression kinematic of a bivalve. Our propulsor generates a non-linear time-varying exit velocity profile by compressing and relaxing a flexible bulb with two rigid arms and has a finite volume capacity. The formation process of the vortices generated by this jet profile is analysed using time-resolved velocity field measurements. The temporal evolution of the vortex topology and its integral quantities are analysed based on the finite-time Lyapunov exponent field and the pressure field, both derived from the velocity data.

When fluid is ejected by our vortex propulsor, a coherent vortex ring is formed. This primary vortex ring rapidly moves away from the nozzle exit during the compression phase and a trailing shear layer with a secondary vortex emerges. The secondary vortex has a higher translation velocity than the initial primary vortex and both merge before the end of the bulb compression. Analysis of the temporal evolution of the ridge in the FTLE field during vortex pairing reveal that the vortex length increases beyond its diameter pre-pairing due to the lagging of the positive FTLE ridge. During vortex pairing, the vortex length contracts and its diameter increases such that additional vorticity is accepted by the primary vortex ring without changing its non-dimensional energy, in agreement with the Kelvin-Benjamin variational principle. The vortex diameter, circulation, and translational velocity all converge to new post-pairing values post-pairing.

Our Lagrangian analysis provides detailed and accurate insight into the formation and development of the vortex ring generated by the non-linear evolution of the stoke ratio generated by our propulsor. However, this type of analysis is computationally expensive, requires time-resolved flow field data, and can not be conducted in-situ to provide input for optimisation and control of the time-dependent exit velocity profile. An alternative pressure-based methodology does not require time-resolved data and can be applied on a single snapshot. We reveal that the trajectories of the pressure maxima that lead and trail the vortex core coincide with the trajectories of the negative and positive FTLE ridges pre and post vortex pairing. During vortex pairing, the trailing pressure maximum is less pronounced. The local pressure maxima can serve as reliable observables for vortex ring formation and shedding that could be picked up by pressure sensors integrated in the surface around the nozzle exit.

Our results provide novel insights into the evolution of integral quantities of vortex rings during pairing and can aid and inspire the further design and control of underwater vehicles that uses pulsatile jet propulsion.

**Funding Statement.** This work was supported by the Swiss National Science Foundation (grant nr. 200021175792).

**Declaration of Interests.** The authors declare no conflict of interest.

**Data Availability Statement.** The data used in this work will be made available upon request.

## References

- Benjamin, T. B. (1976). The alliance of practical and analytical insights into the nonlinear problems of fluid mechanics. In P. Germain & B. Nayroles, editors, *Applications of Methods of Functional Analysis to Problems in Mechanics. Lecture Notes in Mathematics*, volume 503 of *Lecture Notes in Mathematics*, pages 8–29. Springer. ISBN 9783540076292.
- Gharib, M., Rambod, E., & Shariff, K. (1998). A universal time scale for vortex ring formation. *Journal of Fluid Mechanics*, 360, 121–140, 0022-1120, 1469-7645.
- Mohseni, K. & Gharib, M. (1998). A model for universal time scale of vortex ring formation. *Physics of fluids*, 10(10), 2436, 1070-6631.
- Rosenfeld, M., Rambod, E., & Gharib, M. (1998). Circulation and formation number of laminar vortex rings. *Journal of Fluid Mechanics*, 376, 297–318, 0022-1120, 1469-7645.

- Zhou, J., Adrian, R. J., Balachandar, S., & Kendall, T. M. (1999). Mechanisms for generating coherent packets of hairpin vortices in channel flow. *Journal of Fluid Mechanics*, 387, 353–396, 1469-7645.
- Whitcomb, L., Yoerger, D. R., Singh, H., & Howland, J. (2000). Advances in Underwater Robot Vehicles for Deep Ocean Exploration: Navigation, Control, and Survey Operations. In J. M. Hollerbach & D. E. Koditschek, editors, *Robotics Research*, pages 439–448. Springer London, London. ISBN 978-1-4471-0765-1.
- Zhao, W., Frankel, S. H., & Mongeau, L. G. (2000). Effects of trailing jet instability on vortex ring formation. *Physics of Fluids*, 12(3), 589–596, 1070-6631, 1089-7666.
- Haller, G. (2001). Lagrangian structures and the rate of strain in a partition of two-dimensional turbulence. *Physics of Fluids*, 13(11), 3365–3385, 1070-6631, 1089-7666.
- Nitsche, M. (2001). Self-similar shedding of vortex rings. *Journal of Fluid Mechanics*, 435, 397–407, 1469-7645.
- Haller, G. (2002). Lagrangian coherent structures from approximate velocity data. *Physics of Fluids*, 14(6), 1851–1861, 1070-6631, 1089-7666.
- Krueger, P. S. & Gharib, M. (2003). The significance of vortex ring formation to the impulse and thrust of a starting jet. *Physics of Fluids*, 15(5), 1271–1281, 1070-6631, 1089-7666.
- Dabiri, J. O. & Gharib, M. (2004). Delay of vortex ring pinch-off by an imposed bulk counterflow. *Physics of fluids*, 16(4), L28–L30, 1070-6631.
- Dabiri, J. O. & Gharib, M. (2005). Starting flow through nozzles with temporally variable exit diameter. *Journal of Fluid Mechanics*, 538, 111–136, 1469-7645.
- Dabiri, J. O. (2006). Fast-swimming hydromedusae exploit velar kinematics to form an optimal vortex wake. *Journal of Experimental Biology*, 209(11), 2025–2033, 0022-0949, 1477-9145.
- Krueger, P. S., Dabiri, J. O., & Gharib, M. (2006). The formation number of vortex rings formed in uniform background co-flow. *Journal of Fluid Mechanics*, 556, 147, 1469-7645.
- Mohseni, K. (2006). Pulsatile vortex generators for low-speed maneuvering of small underwater vehicles. *Ocean Engineering*, 33(16), 2209–2223, 00298018.
- Shadden, S. C., Dabiri, J. O., & Marsden, J. E. (2006). Lagrangian analysis of fluid transport in empirical vortex ring flows. *Physics of Fluids*, 18(4), 047105, 1070-6631, 1089-7666.
- Shusser, M., Rosenfeld, M., Dabiri, J. O., & Gharib, M. (2006). Effect of time-dependent piston velocity program on vortex ring formation in a piston/cylinder arrangement. *Physics of fluids*, 18(3), 033601, 1070-6631.
- Green, M. A., Rowley, C. W., & Haller, G. (2007). Detection of Lagrangian coherent structures in three-dimensional turbulence. *Journal of Fluid Mechanics*, 572, 111–120, 0022-1120, 1469-7645.
- Shadden, S. C., Katija, K., Rosenfeld, M., Marsden, J. E., & Dabiri, J. O. (2007). Transport and stirring induced by vortex formation. *Journal of Fluid Mechanics*, 593, 315–331, 0022-1120, 1469-7645.
- Akhmetov, D. G. (2009). *Vortex Rings*. Springer Berlin Heidelberg, Berlin, Heidelberg. ISBN 978-3-642-05015-2 978-3-642-05016-9.
- Dabiri, J. O. (2009). Optimal Vortex Formation as a Unifying Principle in Biological Propulsion. *Annual Review of Fluid Mechanics*, 41(1), 17–33, 0066-4189, 1545-4479.
- Green, M. A., Rowley, C. W., & Smits, A. J. (2010). Using hyperbolic Lagrangian coherent structures to investigate vortices in bioinspired fluid flows. *Chaos: An Interdisciplinary Journal of Nonlinear Science*, 20(1), 017510, 1054-1500, 1089-7682.
- Olcay, A. B. & Krueger, P. S. (2010). Momentum evolution of ejected and entrained fluid during laminar vortex ring formation. *Theoretical and Computational Fluid Dynamics*, 24(5), 465–482, 0935-4964.
- O’Farrell, C. & Dabiri, J. O. (2010). A Lagrangian approach to identifying vortex pinch-off. *Chaos: An Interdisciplinary Journal of Nonlinear Science*, 20(1), 017513, 1054-1500, 1089-7682.
- Buchmann, N., Willert, C., & Soria, J. (2012). Pulsed, high-power led illumination for tomographic particle image velocimetry. *Experiments in Fluids*, 53, 1545–1560.
- Lawson, J. M. & Dawson, J. R. (2013). The formation of turbulent vortex rings by synthetic jets. *Physics of Fluids*, 25(10), 105113, 1070-6631, 1089-7666.
- Zahugi, E. M. H., Shanta, M. M., & Prasad, T. V. (2013). Oil Spill Cleaning Up Using Swarm of Robots. In N. Meghanathan, D. Nagamalai, & N. Chaki, editors, *Advances in Computing and Information Technology*, pages 215–224. Springer Berlin Heidelberg, Berlin, Heidelberg. ISBN 978-3-642-31600-5.
- Dabiri, J. O., Bose, S., Gemmell, B. J., Colin, S. P., & Costello, J. H. (2014). An algorithm to estimate unsteady and quasi-steady pressure fields from velocity field measurements. *Journal of Experimental Biology*, 217(3), 331–336, 0022-0949, 1477-9145.
- Weymouth, G. D., Subramaniam, V., & Triantafyllou, M. S. (2015). Ultra-fast escape maneuver of an octopus-inspired robot. *Bioinspiration & Biomimetics*, 10(1), 016016, 1748-3190.
- Schlueter-Kuck, K. & Dabiri, J. O. (2016). Pressure evolution in the shear layer of forming vortex rings. *Physical Review Fluids*, 1(1), 012501, 2469-990X.
- Bayat, B., Crasta, N., Crespi, A., Pascoal, A. M., & Ijspeert, A. (2017). Environmental monitoring using autonomous vehicles: a survey of recent searching techniques. *Energy biotechnology • Environmental biotechnology*, 45, 76–84, 0958-1669.
- Krishna, S., Green, M. A., & Mulleners, K. (2018). Flowfield and force evolution for a symmetric hovering flat-plate wing. *AIAA Journal*, 56(4), 1360–1371.
- Robertson, M. A., Lfremov, F., & Paik, J. (2019). RoboScallop: A Bivalve Inspired Swimming Robot. *Ieee Robotics And Automation Letters*, 4(2), 2078–2085.

- Zhu, J., White, C., Wainwright, D. K., Santo, V. D., Lauder, G. V., & Bart-Smith, H. (2019). Tuna robotics: A high-frequency experimental platform exploring the performance space of swimming fishes. *Science Robotics*, 4(34), eaax4615, 2470-9476.
- de Guyon, G. & Mulleners, K. (2021a). Modelling vortex ring growth in the wake of a translating cone.
- de Guyon, G. & Mulleners, K. (2021b). Scaling of the translational velocity of vortex rings behind conical objects. *Physical Review Fluids*, 6(2), 024701, 2469-990X.
- Gemmell, B. J., Dabiri, J. O., Colin, S. P., Costello, J. H., Townsend, J. P., & Sutherland, K. R. (2021). Cool your jets: biological jet propulsion in marine invertebrates. *Journal of Experimental Biology*, 224(12), 0022-0949.
- Limbourg, R. & Nedić, J. (2021). An extension to the universal time scale for vortex ring formation. *Journal of Fluid Mechanics*, 915, A46, 0022-1120.
- Xu, N. W. (2021). Squid-inspired robots perform swimmingly. *Science Robotics*, 6(50), eabf4301, 2470-9476.

## Supplementary Material.

**Experimental set-up.** Figure 10 shows detailed photographs and a schematic of the experimental set-up including the arrangement of the high-speed camera and 45° mirror to image the field of view indicated by the dashed rectangle in Figure 10b). The photograph in Figure 10a shows the vortex propulsor ejecting a vortex ring and the photograph in Figure 10c shows the LED light sheet optics (LED Pulsed System, ILA\_5150 GmbH, Germany).

**Thrust estimation.** An estimate of the propulsive force generated by the bio-inspired device presented here is obtained from a momentum balance directly behind the nozzle exit at  $x/D = 0$ . We assume that the propulsive force experienced by the device is proportional to the mass flow rate of the fluid that is ejected. The average thrust generated over the time of compression is 0.027 N.

**Suggested location of pressure sensors.** The results presented in this paper disclose new opportunities to use local pressure sensors as input for closed loop control of the temporal exit velocity profile to improve the propulsion efficiency of under water vehicles utilising pulsatile jet propulsion. Potential locations of the pressure sensors integrated in the surface around the nozzle exit are presented in Figure 11a. The predicted sensor output based on the pressure field computed from the measured velocity field is presented in Figure 11b. The pressure signals indicated a clear drop around  $L/D = 2$  when the primary vortex ring moves away from the nozzle and the non-dimensionalised energy has converged to its final value.

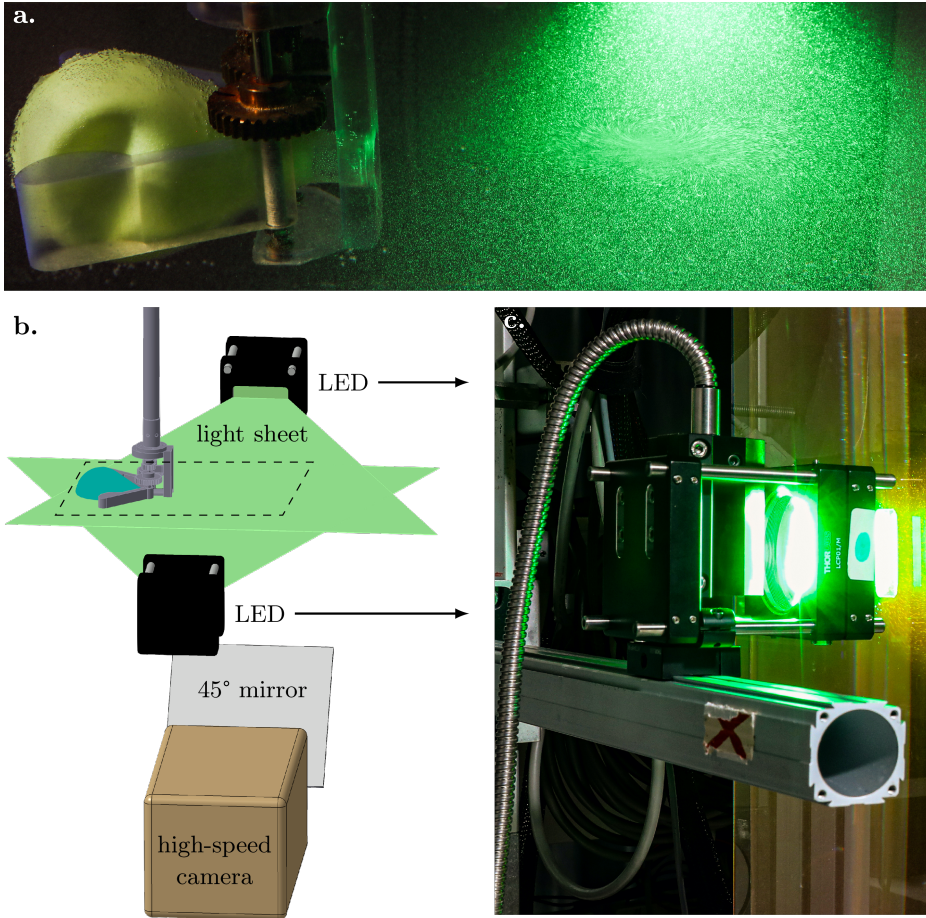


**Figure 10.** (a) Photograph of the compressing propulsor and the ejected vortex ring. (b) Schematic of the experimental set-up including the arrangement of the high-speed camera, 45° mirror, and light sheet optics with respect to the vortex propulsor. (c) Photograph of the LED light sheet optics.

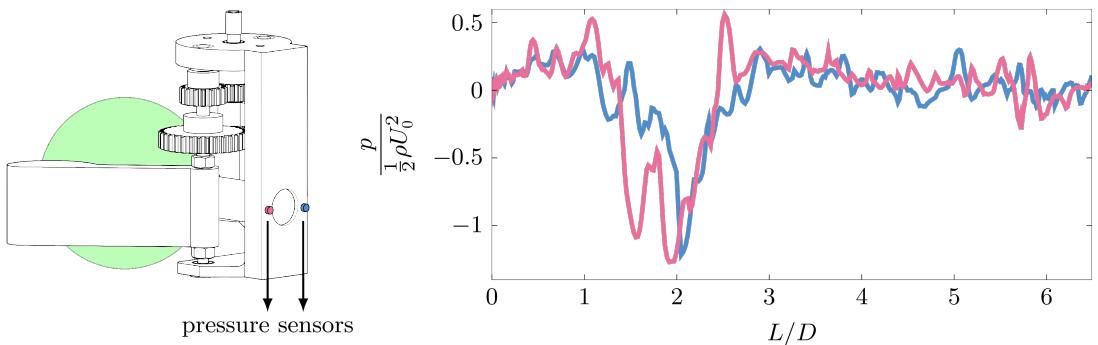


**Figure 11.** (a) Potential locations of integrated pressure sensors to provide input for future closed loop control of the temporal exit velocity profile. (b) Hypothetical temporal evolution of the pressure signatures captured at these two locations, obtained from the pressure field which was derived directly for the measured velocity field data.